Journal of Alloys and Compounds 572 (2013) 5–10

Contents lists available at SciVerse ScienceDirect

Journal of Alloys and Compounds

journal homepage: www.elsevier.com/locate/jalcom

Microstructure and precipitates in annealed $Co_{38}Ni_{33}Al_{29}$ ferromagnetic shape memory alloy

J.B. Lu [a,*], H. Shi [a], S. Sedlakova-Ignacova [c], R. Espinoza [a], J. Kopeček [c], P. Sittner [c], B. Bártová [a,b], D. Schryvers [a]

[a] EMAT, University of Antwerp, Groenenborgerlaan 171, B-2020 Antwerp, Belgium
[b] CIME&LSME, École Polytechnique Fédérale de Lausanne, Station 12, Lausanne CH-1015, Switzerland
[c] Department of Functional Materials, Institute of Physics ASCR v.v.i., Na Slovance 2, Prague 8 CZ-182 21, Czech Republic

ARTICLE INFO

Article history:
Received 11 January 2013
Received in revised form 8 March 2013
Accepted 25 March 2013
Available online 2 April 2013

Keywords:
Ferromagnetic shape memory alloy
Precipitation
Microstructure
TEM
FIB/SEM

ABSTRACT

Transmission electron microscopy was performed to investigate the microstructure and precipitates in the annealed $Co_{38}Ni_{33}Al_{29}$ ferromagnetic shape memory alloy. Apart from the dendritic secondary phase in the austenite matrix, micron-sized (up to 100 μm) fcc-based precipitates with partial γ′ $L1_2$ ordering and containing none, one or three $\{1\,1\,1\}_p$ parallel twin planes were found. The orientation relationship between the precipitates and matrix was found to be Kurdjumov–Sachs. STEM–EDX analysis indicates that twinned and non-twinned precipitates are Co-rich and Al- and Ni-deficient with respect to the matrix and with a lower Co/Al ratio for the latter. The 3D morphologies of precipitates were reconstructed with focused ion beam/scanning electron microscope dual-beam slice-and-view imaging, showing that the single $\{1\,1\,1\}_p$ plane twinned precipitates have a plate-like shape while the non-twinned precipitates are lath-like and often bent.

1. Introduction

Shape memory alloys (SMAs) have attracted considerable attention because of their potential applications in industry as sensors and compact actuators and in medicine as self-expanding stents, orthodontic and orthopedic devices, etc. [1–3]. For conventional SMAs, the shape memory effect is induced by means of changes in either temperature or stress or both. In ferromagnetic shape memory alloys (FSMAs) the shape memory and related effects can be triggered not only by the temperature and stress, but also by changes in an external magnetic field [4].

One well-known shape memory system is paramagnetic Ni–Al in which the austenite β-phase has a cubic B2 structure [5]. With replacing Ni by Co this paramagnetic alloy changes into a ferromagnetic Co–Ni–Al SMA [6,7], which is also viewed as a high temperature SMA as a result of its increased transformation temperatures [8], an extra potential advantage over the conventional binary system. The B2 structure of the Co–Ni–Al austenite alloy undergoes a martenstic transformation into a tetragonal $L1_0$ martensitic phase [9]. The martensitic transformation temperatures (start M_s or other) and magnetic Curie temperature (T_c) can individually be controlled by changing the concentrations of Co and Al [6]. However, it is reported that Co–Ni–Al material only consisting of single β-phase exhibits very poor ductility [6]. The introduction of a eutectic secondary phase can improve the hot fabricability and the high temperature ductility [6,10,11], which implies an important advantage for practical applications. With these properties in mind the as-cast single crystal $Co_{38}Ni_{33}Al_{29}$ ferromagnetic SMA was studied by transmission electron microscopy (TEM) a few years ago [12]. Besides the eutectic secondary phase in the austenite matrix, nano-sized Co-rich precipitates were also observed, and the crystallographic relationship between larger nano-sized precipitates and matrix was found to be close to the Kurdjumow–Sachs (K–S) relationship. In order to investigate the evolution of the microstructure and precipitates influenced by different heat treatments, the as-cast samples were annealed at 1373 K for 72 h and followed by water quenching. On the other hand, in the Co–Ni–Al system it is also reported that the hardness of the alloy is affected by the heat treatment due to the presence of the precipitates [13]. From metallographic aspect, the shape, crystal structure and orientation relationship of precipitates play an important role in the behavior of the alloy. In the present study, the microstructure, morphology and chemical composition of the precipitates of the annealed sample will be investigated with conventional and analytical TEM. The 3D morphologies of different precipitates will also be revealed with focused ion beam (FIB)/scanning electron microscope (SEM) dual-beam slice-and-view imaging technique.

* Corresponding author. Tel.: +32 32653731.
E-mail address: jblu10@gmail.com (J.B. Lu).

0925-8388/$ - see front matter © 2013 Elsevier B.V. All rights reserved.
http://dx.doi.org/10.1016/j.jallcom.2013.03.228

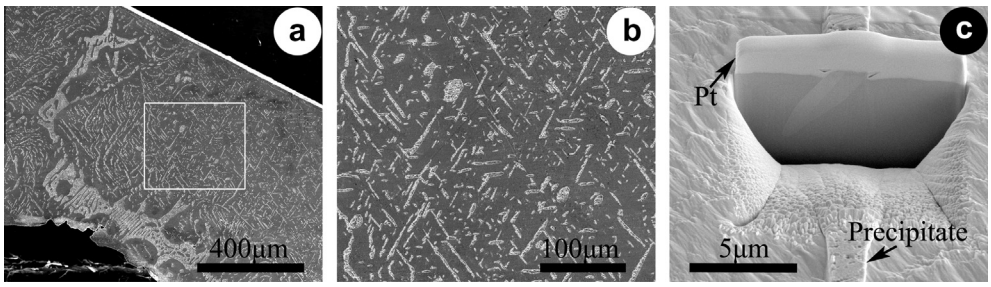

Fig. 1. (a) SEM image of the BM2 bulk sample revealing the overall microstructure of the alloy. (b) Enlarged image of the rectangle in (a) showing the distribution and surface cross-section morphologies (rod- and ellipse-like) of the precipitates in the matrix. (c) High magnification SEM image of a FIB cut from a precipitate revealing a plate-like morphology with a central interface.

2. Materials and methods

The $Co_{38}Ni_{33}Al_{29}$ ingot was obtained from Special Metals Corporation (New Hartford, NY). The ingot was melted and single crystals were grown by the directional Bridgman technique with a pulling rate of 7.7 μm s^{-1} in an Ar atmosphere [14]. The as-cast sample, labeled BM1, was then annealed at 1373 K in vacuum for 72 h and followed by water quenching. The annealed sample is labeled BM2 (see Table 1).

Conventional TEM samples were prepared by twin-jet electropolishing in a 20% sulfuric acid and 80% methanol electrolyte at 258 K [12]. The SEM observation, FIB cut and slice-and-view 3D imaging were carried out on an FEI Helios NanoLab 650 Dual Beam FIB/SEM system consisting of a standard ion column which allows Ga^+ cleaning and milling in a range of 500 V–30 kV. To clearly observe the microstructure of the bulk sample with SEM, the sample was etched in 50 ml H_2O, 50 ml HCl and 10 g $CuSO_4$ solution for 10 s. Conventional TEM was carried out on a LaB_6 Philips CM20, while the high-resolution TEM and analytical scanning TEM (STEM)–energy dispersive X-ray (EDX) analysis was performed on a FEI FEG Tecnai G^2, both microscopes operating at 200 kV.

3. Results

3.1. Transmission electron microscopy

The microstructure of the as-cast BM1 sample was studied before by conventional and advanced TEM [12]. Besides the dendritic secondary phases coexisting with the austenite matrix and grown from the eutectic phase transition, nano-sized precipitates ranging from 5 to 25 nm in diameter were observed. The orientation relationship between the larger of these nano-sized precipitates and the B2 matrix was confirmed to be close to the K–S relationship. The smaller precipitates were found to be faceted. Energy filtered TEM revealed that the precipitates are enriched in Co with respect to the matrix.

In the annealed BM2 sample, aside from the dendritic secondary phases dispersed in the austenite matrix, many micron-sized rod-like precipitates were found in the matrix and revealing a Widmanstätten-like structure as shown in the SEM image of Fig. 1a [9,15]. Fig. 1b shows the enlarged image of the rectangle in Fig. 1a. Apart from the rod-like precipitates, several ellipse-shaped (or elongated polygon) precipitates are observed. Moreover, at the left hand side of Fig. 1b, close to the eutectic structure, some curved rod-like precipitates can be seen. The precipitates in the BM2 sample are much larger than the ones in the BM1 sample, but their true 3D dimensions are difficult to judge from a simple SEM image. However, from the FIB cross-section of a straight rod-like precipitate shown in Fig. 1c they are estimated to have a plate-like shape several (5–10) μm wide, 1–2 μm thick and sometimes up to 100 μm long. From the contrast in this image it is also clear that a central interface exists parallel to the largest surface of the plate.

Fig. 2a shows the BF image of six relatively small precipitates in the BM2 sample. Selected area electron diffraction (SAED) in Fig. 2c–f confirm an fcc-based crystal structure for the precipitates. Moreover, weak ordering reflections are observed indicating at least partial γ′ $L1_2$ type ordering. The BF image in Fig. 2a was taken along the $[1\,1\,0]_p$ of precipitate-1 (“p” denotes the precipitate, “a” stands for the cubic austenite matrix). Four of the precipitates are labeled with numbers in order to illustrate their relative orientation relationships. Typical dimensions for these precipitates are 2 or 3 μm in thickness and a few microns in length (i.e., on the small end of the distribution scale when compared with the SEM image of Fig. 1). Fig. 2b shows the BF image of precipitate-1 at a higher magnification (several degrees off to the $[1\,1\,0]_p$ zone axis to enhance twin contrast) revealing a single $(-1\,1\,1)_p$ twin plane along the central axis. It is noted that precipitate-1 contains a re-entrant groove at one tip as indicated by the white arrow, which provides a preferential crystal growth site with low energy barrier for atom attachment [16–18]. Fig. 2c shows the corresponding SAED pattern of the twinning structure in Fig. 2b. Fig. 2d shows the SAED pattern taken along the $[1\,1\,0]_p$ zone axis of precipitate-1 from its interface with the austenite matrix as indicated by the black arrow in Fig. 2b. The latter confirms not only the K–S orientation relationship between the two structures i.e., $[1\,1\,1]_a//[1\,1\,0]_p$, $(-1\,1\,0)_a//(-1\,1\,1)_p$ but also shows that precipitate-1 is elongated along its $[1\text{–}12]_p$ direction (=$[-1\,-1\,2]_a$). Fig. 2e shows the SAED pattern from the region indicated by the white circle in Fig. 2b and thus consists of the diffraction patterns shown in Fig. 2c and d, i.e., containing the twinned precipitate as well as the austenite matrix. Fig. 2f shows the diffraction pattern taken from the area as indicated by the white circle in Fig. 2a containing the twinned precipitate-1, twinned precipitate-4 and austenite matrix. The white arrows in Fig. 2f indicate the diffraction spots from the twinning structures of both precipitates. From Fig. 2f we can measure an angle of 60° between the twin planes of precipitate-1 and -4, confirming the measurement in Fig. 2a. Twin plane orientation relationships between precipitates-1, -2 and -3 were also examined from their diffraction patterns relative to the diffraction pattern of the matrix, confirming the correspondence of the $\{1\,1\,1\}_p$ twin planes with the corresponding $\{1\,1\,0\}_a$ austenite planes as well as the full K–S orientation relationship. The contrast inside the long unlabeled precipitate also observed in Fig. 2a indicates a twin plane inclined to the viewing direction, which was confirmed after tilting the specimen. From the relative orientation relationships, it can thus be concluded that the twinned rod-shaped precipitates in the BM2 sample have a specific orientation distribution, possibly due to the existence of the $\{1\,1\,1\}_p$ twin planes inside the precipitates, while the precipitate and matrix crystal structures have a K–S orientation relationship.

Although most of the γ′ precipitates contain only one single twinning plane, Fig. 3a shows the $[1\,1\,0]_p$ (=$[1\,1\,1]_a$) zone axis BF image of a precipitate containing three parallel $\{1\,1\,1\}_p$ twinning planes. The corresponding SAED pattern taken from the whole area, i.e. including the surrounding matrix, is shown in the lower-right corner and is similar to the SAED in Fig. 2e. The inset in the lower-left corner shows the enlarged image of the lower-left

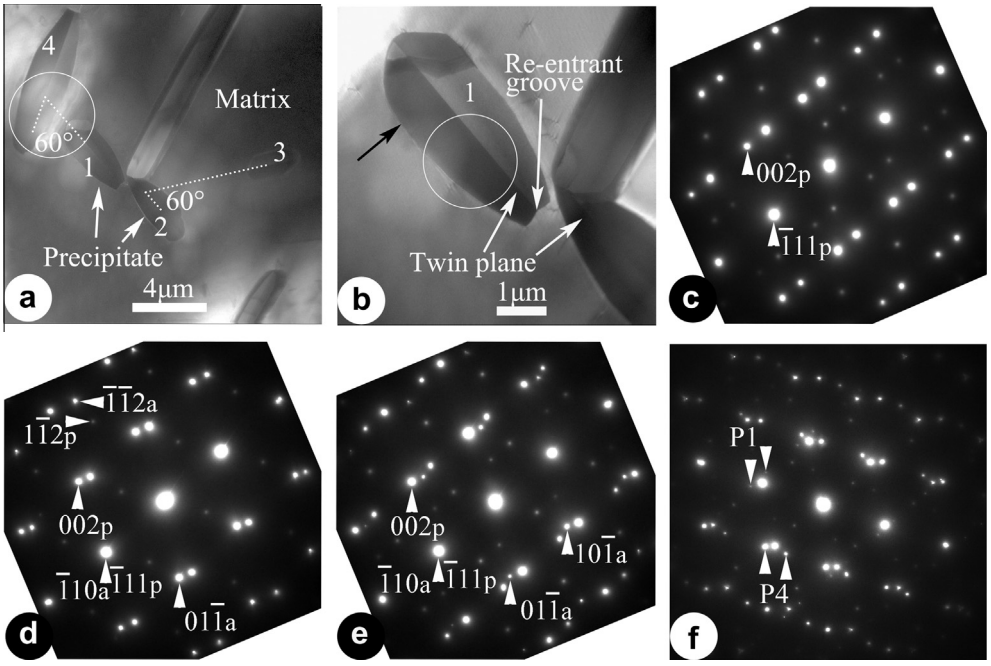

Fig. 2. TEM study of the precipitates in the BM2 sample. (a) BF image of six precipitates taken along the $[1\,1\,0]_p$ zone axis of precipitate-1 (i.e., $[1\,1\,1]_a$ of matrix). (b) BF image of precipitate-1 at higher magnification (several degree off to the $[1\,1\,0]_p$). (c) $[1\,1\,0]_p$ zone axis SAED of precipitate-1 from the twinning region. (d) $[1\,1\,0]_p$ zone axis SAED of precipitate-1 from the interface of precipitate-1 and matrix as indicated by the black arrow in (b) showing the K–S orientation relationship. (e) $[1\,1\,0]_p$ SAED of precipitate-1 from the region indicated by the white circle in (b). (f) $[1\,1\,0]_p$ SAED of precipitate-1 from the region indicated by the white circle in (a) (the major spots are from the $[1\,1\,1]_a$ matrix).

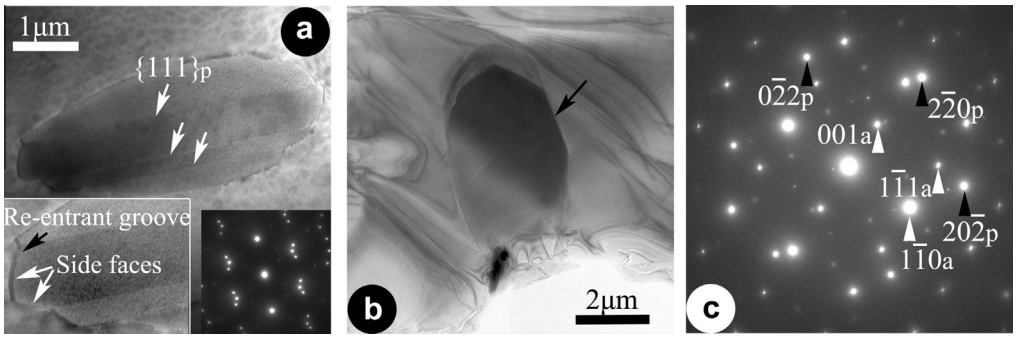

Fig. 3. (a) BF image of a triple $\{1\,1\,1\}_p$ twinned precipitate observed along the $[1\,1\,0]_p$ zone axis of the precipitate with the enlarged image of one tip and corresponding SAED as insets. (b) Shows the BF image of a precipitate taken along its $[1\,1\,1]_p$ zone axis (i.e., $[1\,1\,0]_a$). (c) Corresponding SAED taken at the black arrow position in (b) (weak spots around the main reflection spots are due to double diffraction).

tip of the precipitate indicating the mixed side-face structure. The black arrow indicates a small re-entrant groove and the two white arrows indicate the side faces between the twin planes. Fig. 3b shows the BF image of a precipitate taken along the $[1\,1\,1]_p$ zone axis (i.e., the normal to the twin plane) revealing a close to faceted plate shape of the precipitate. Fig. 3c shows the corresponding SAED taken at the black arrow in Fig. 3b and including some double diffraction (weak spots around the main reflection spots). The observed cross-sections of the precipitates in Fig. 2a reveal that the major parts of the flat edges are parallel with the internal central twin planes, i.e. close-packed $\{1\,1\,1\}_p$ planes. It has been reported that the precipitates in Co–Ni–Al system grow along a $\langle 1\,1\,1\rangle_a$ direction since the misfit between the B2 matrix and fcc-Co precipitates are minimum (0.5%) in the $\langle 1\,1\,1\rangle_a$ direction of the B2 matrix [13], which is consistent with our observation in Fig. 3b that the long axis of the prolonged plate-like precipitate is along the $[-1\,1\,1]_a$ direction. The faceted edges observed in Fig. 3b might be due to the truncation of the polyhedron shape of the precipitate. This view confirms the approximate ellipse-like (or elongated polygon) shapes in the SEM image Fig. 1b.

Apart from the twinned precipitates, a few precipitates free of twinning are also observed. Fig. 4 shows the BF image of a precipitate without twinning and observed along the $[1\,1\,1]_a$ of the matrix (i.e., $[1\,1\,0]_p$). The inset shows the corresponding SAED from the precipitate and matrix confirming the partial $L1_2$ ordering by weak superreflections and a K–S orientation relationship. Compared with the twinned precipitates, no re-entrant grooves at the short edges of the precipitate are found.

3.2. Chemical analysis

Chemical concentration gradients across the phase boundaries were found to strongly affect the mechanical properties of SMA such as in precipitation-hardened maraging TRIP steel [19] and Ni–Ti multi-layer films [20]. In the present work, the chemical information across the interfaces between the precipitates and

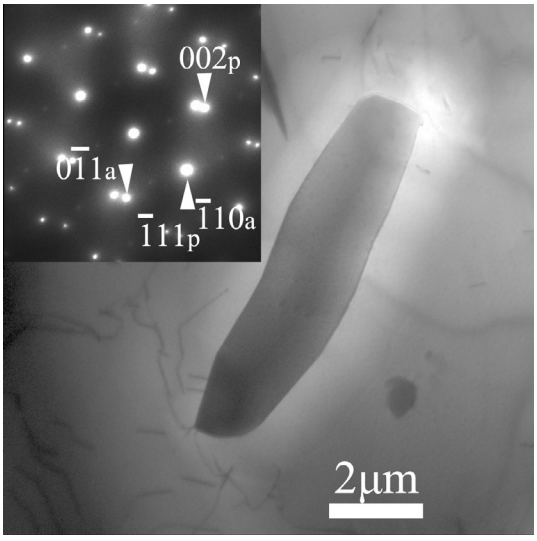

Fig. 4. BF image of a precipitate without twinning. Inset shows the corresponding SAED pattern from the precipitate and matrix confirming the K–S orientation relationship.

austenite was studied by STEM–EDX line scan analysis. Fig. 5a shows the STEM image of a single twinned precipitate while Fig. 5b shows the STEM line scan EDX profiles of the three occurring elements. Table 2 shows the quantitative concentrations obtained from the element profiles, including thickness correction and illustrating that the single twinned precipitate is Co-rich and Al- and Ni- deficient with respect to matrix, as expected. As seen in Fig. 5b no clear chemical gradient zone in the austenitic matrix was observed. STEM–EDX analyses were also performed to investigate the chemical information of non-twinned precipitates (Table 3). Compared to the data in Table 2, the compositions of both matrices are nearly the same, but the Co concentration is 6.7% lower and the Al concentration is 31% higher in the non-twinned precipitate, while the Ni concentration is almost identical in both kinds of precipitates.

3.3. Slice-and-view (FIB/SEM) study

Although some indications of the 3D plate-like shape of the precipitates were already given above, in the following slice-and-view (FIB/SEM) is used to further document the 3D morphology of the precipitates [21,22]. The cutting ion beam was operated at 30 kV, 9.5 nA and the imaging electron beam at 5 kV, 1.6 nA. The thickness of the slice cut off is 100 nm.

Fig. 6a and b show the reconstructed images of a relatively large and single twinned precipitate viewed from different directions. From the measured primary dimensions we can confirm that the precipitate has a plate-like shape, whereas most SEM and TEM images reveal a "rod-like" shape. Moreover, it is confirmed that the major parts of the large faces of the precipitate are parallel to the internal twinning plane. Fig. 6c shows one of the cross-section SEM images of the precipitate used for the reconstruction and revealing the single twin internal structure. It is noted that the re-entrant groove of the single twinned precipitate has vanished because of the preferential growth at the groove by which only slow-growing protruding facets are retained [16,23].

Fig. 7a–c show the reconstructed images of a non-twinned precipitate viewed along different directions. Fig. 7d shows one of the cross-section SEM images of the precipitate used for the 3D reconstruction, revealing the absence of twinning inside the precipitate. In contrast to the large flat side faces parallel to the twinning plane in Fig. 6, it is clear from Fig. 7b that the side faces of the non-twinned precipitate are a bit curved. Moreover, the 3D shape of this precipitate is more lath-like with one very long axis. The curvature of the non-twinned precipitate confirms the SEM observations in Fig. 1b of some curved precipitates at the left side of the image.

4. Discussion

The above results follow our earlier conclusions on as-cast and shortly annealed samples of the same system [12,24]. The nano-precipitates observed in those studies have grown to micron-sized precipitates presented here. The morphology of a non-twinned precipitate in alloys induced by aging treatment is known to be generally dominated by its crystal structure, its misfit with the matrix and the resulting structure of the interphase boundary. The growth of the precipitate generally follows the direction of the lowest interface misfit, and there is no preferential site to increase the growth rate. Under different circumstances non-twinned rod- or needle-shaped precipitates have been reported in the present system before. In recent work by Oh et al. hexagonal $(Ni,Co)_2Al$ phase precipitates with needle- or rod-like shapes and up to 1 μm in length were observed in samples annealed at lower temperatures than in the present work [25]. Tian et al. observed micron-sized hcp- and fcc-based Co-rich rod-shaped precipitates when annealing the system at higher temperatures [13]. Although

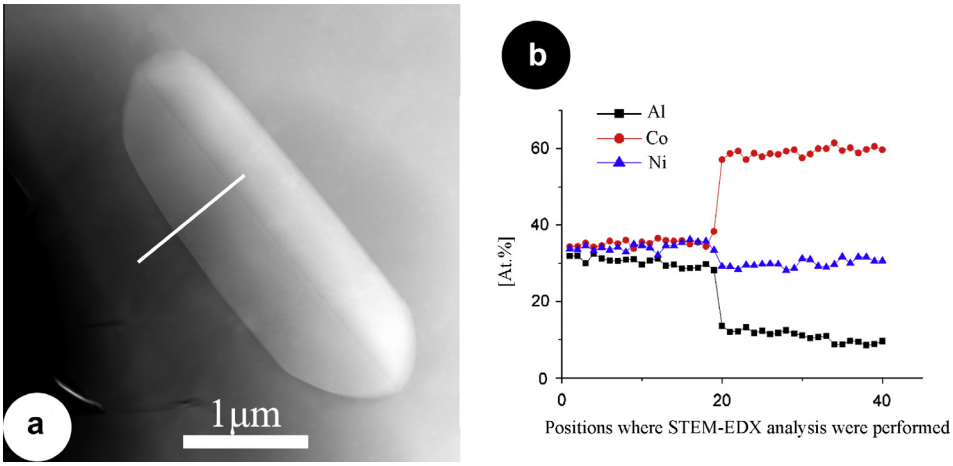

Fig. 5. (a) STEM image of a single twinned precipitate. (b) EDX concentration profiles of Co, Ni and Al across the precipitate–matrix interface.

Table 1
Pulling rates, annealing temperature and time for the studied materials.

	Pulling rate (μm s^{-1})	Annealing temperature and time (K/h), followed by water quenching
BM1	7.7	As-cast
BM2	7.7	1373/72

Table 2
Quantitative concentrations obtained from the element profiles in Fig. 5b, including statistical standard error values.

	Co (at.%)	Ni (at.%)	Al (at.%)
Matrix	35.21 ± 0.18	34.34 ± 0.25	30.44 ± 0.27
Precipitate	59.12 ± 0.24	29.93 ± 0.23	10.94 ± 0.33

Table 3
Quantitative concentrations obtained from the non-twinned precipitate in Fig. 4 using STEM–EDX analysis, including statistical standard error values.

	Co (at.%)	Ni (at.%)	Al (at.%)
Matrix	35.02 ± 0.33	35.15 ± 0.26	29.82 ± 0.32
Precipitate	55.13 ± 0.55	30.51 ± 0.39	14.35 ± 0.37

the latter work also concluded the K–S relationship between the fcc precipitates and the B2 matrix, no $L1_2$ ordering was observed and no twinning inside the precipitates was concluded (although the contrast in the rod of Fig. 8a in Ref. [13] could possibly be due to internal twinning). In both of the above cases, the long axis of the rod was seen to grow in the ⟨1 1 1⟩ direction of the B2 matrix, following the direction of the lowest interface strain, similar to the lens-shape of Ni_4Ti_3 precipitates playing an essential role in the functional behavior of SMA alloys of the Ni–Ti system [26,27]. In the latter case the change in interplanar spacing in the direction perpendicular to the central plane of the precipitate induces a strain gradient in the matrix further hindering the growth of the precipitate in this direction. The non-twinned $L1_2$ precipitates observed in the present system also primarily reveal rod-like shapes, confirming the earlier work.

The situation of twinned precipitates is usually quite different. For example, in the Al–Ge alloy system, the morphologies of the Ge precipitates, growing with the diamond structure inside the Al fcc matrix, are directly related to the number and type of internal twin structures [23]. Triangular plate-shaped precipitates contain only one twinning plane while hexagonal plate-shaped precipitates contain two or more parallel twinning planes. The occurrence of a twin plane results in dense and slow growing $(1\,1\,1)_{fcc}$ surface planes parallel to the twin plane of the precipitates meanwhile forming re-entrant surface grooves at twin junctions yielding preferential sites with low energy barriers for atom attachment. In the present case re-entrant grooves were observed in Figs. 2b and 3a. It can thus be concluded that the existence of a single $\{1\,1\,1\}_p$ twin plane yielding re-entrant grooves at three of the edges of a precipitate plus the K–S relationship between precipitate and matrix result in the formation of flat plate-like precipitates. The rod-like shapes observed with 2D SEM and TEM can thus be interpreted as (mechanical and electro)-polished cross-sections of these 3D plate forms.

A note needs to be added on the occurrence of the $L1_2$ ordering. Since the corresponding superreflections are relatively weak and even look somewhat diffuse the precipitates are not considered to being completely ordered. Although every attempt was made to ensure a rapid quench avoiding diffusion, this partial ordering could have occurred during quenching. In Ref. [9] the XRD spectrum obtained from a Ni–33Co–28Al alloy after quenching from 1473 K also reveals a small (1 0 0) peak, indicating partial $L1_2$ ordering.

The reason why twinned as well as non-twinned precipitates exist in the present annealed alloy can possibly be related with the strong difference in Co/Al ratio, as concluded from the EDX

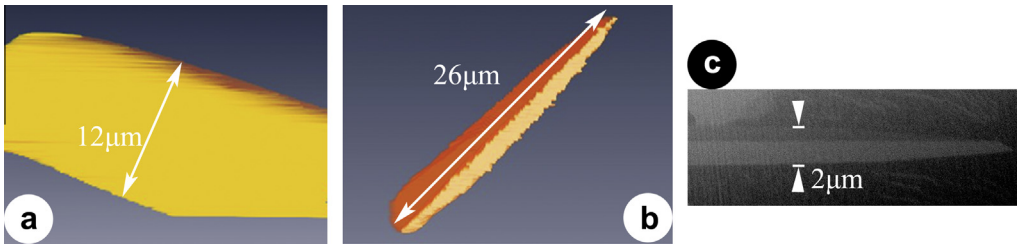

Fig. 6. (a and b) The reconstructed images of a single twinned precipitate viewed along different directions. (c) One of the SEM images used for reconstruction revealing the twinning structure in the precipitate.

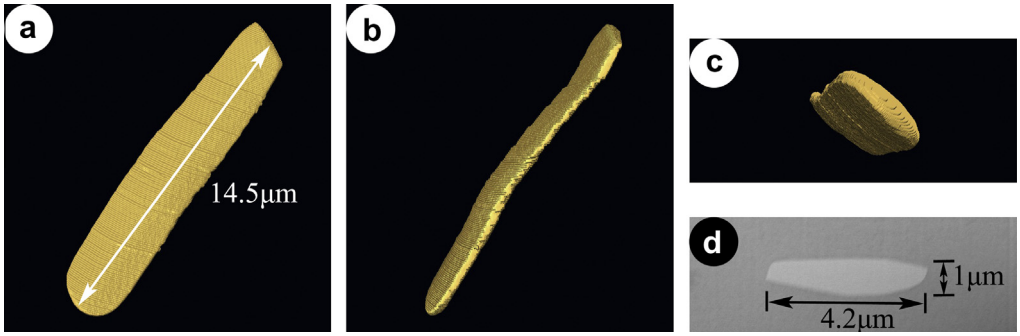

Fig. 7. (a–c) Reconstructed images of a non-twinned precipitate viewed along different directions. (d) One of the SEM images used for the reconstruction revealing the twin-free structure.

measures. Large as-grown single crystals of the Co–Ni–Al system are indeed prone to concentration inhomogeneities in the matrix [14,28], but more likely concentration gradients induced by the formation of the eutectic regions will influence the concentration of the precipitates grown close or far away from these regions. In other words, precipitates observed close to the Co-rich and Al-poor eutectic regions (non-twinned ones) will contain less Co and more Al than precipitates in the central areas of the matrix (twinned ones). Such concentration differences can stabilize different lattice planes of the precipitate structure, locally change elastic properties as well as lattice parameters thus giving rise to different energy competing conditions with the surrounding matrix favoring twinned or non-twinned precipitates, depending on the actual concentration.

There still exists some controversy about the nucleation of such twinned precipitates. In the Ni_2AlTi system it was claimed that the nucleation starts at the mid-rib, the twin plane, and grows sideways generating two twin variants [15], whereas in the Al–Ge system it was suggested that non-twinned nano-particles nucleate first as octahedral shapes with a special orientation relationship with the matrix with the twin developing subsequently [23]. In the current investigation, in which a close-packed fcc structure nucleates inside a more open bcc system, many non-twinned Co-rich nano-precipitates were observed in the as-cast BM1 sample together with some bigger ones, still non-twinned, that fit the K–S orientation relationship with the matrix. These might be considered as different stages of precursors to the micron-sized plate-like precipitates in the annealed BM2 sample, which implies that the twins are formed somewhat after the nucleation.

From the above results it is clear that different heat treatments of Co–Ni–Al will result in particular microstructures, which can affect certain mechanical properties such as ductility, hardness, etc. As mentioned above, Tian et al. reported initial age hardening followed by softening or immediate softening depending on the aging temperature of the Co–Ni–Al system [13]. Although no clear conclusions were drawn this evolution could possibly be correlated with the parallel evolution of the precipitation. Precipitation will also affect the structural shape memory behavior. Indeed, the martensitic transformation temperatures will be affected by the matrix concentration balancing that of the volume fraction of the Co-rich and Al-poor precipitates [29] while precipitates can also act as nucleation sites [26,27,30] and/or hamper the transition front thus widening the hysteresis [31]. Preliminary results further indicate that the precipitates are ferromagnetic at room temperature, i.e. their T_c is higher than that of the austenite, and the magnetic domains inside the precipitates depend on their shapes, microstructure and the existence of twin planes. For now, aside from some local deformation of the matrix domains, no unambiguous effects of the internal domains in the precipitates on the ferromagnetic domains appearing in the austenite upon cooling nor in the ensuing martensitic transformation have been observed, but further work will be necessary to provide complete answers. These results can be expected to be of interest for future work on these alloys when they are further investigated for their potential use as advanced high temperature engineering or magnetic shape memory materials.

5. Conclusions

Transmission and scanning electron microscopy as well as analytical techniques were used to investigate the microstructure and chemical composition of precipitates in a $Co_{38}Ni_{33}Al_{29}$ ferromagnetic shape memory alloy which was grown with a pulling rate of 7.7 $\mu m\,s^{-1}$ and annealed at 1373 K for 72 h. Compared to the as-cast sample obtained from the same single crystal, besides the dendritic secondary phase, many micron-sized non-twinned, single and triple $\{1\,1\,1\}_p$ twinned precipitates with partial γ' $L1_2$ ordering were observed in the austenite matrix. The orientation relationship between precipitates and matrix was determined to be the Kurdjumov–Sachs orientation relationship. STEM–EDX analysis indicates that twinned and non-twinned precipitates are Co-rich and Al- and Ni-deficient with respect to the matrix and with a lower Co/Al ratio for the latter, a difference possibly related with the site of precipitation with respect to the eutectic regions. A 3D morphology investigation of precipitates with FIB/SEM slice-and-view imaging revealed that the single $\{1\,1\,1\}_p$ twinned precipitates have a plate-like shape with flat $\{1\,1\,1\}$ faces while the non-twinned precipitates have a lath-like shape and can be curved.

Acknowledgements

B. Bartova and S. Ignacova thank MULTIMAT "Multi-scale modeling and characterization for phase transformations in advanced materials", an EU Marie Curie Research Training Network (MRTNCT-2004-505226), for supporting this work. R. Espinoza and J.B. Lu thank the Belgian Science ministry (Belspo) for support of their post-doc research stay at EMAT. J. Kopeček also thanks the Czech Science Foundation Project No. P107/10/0824.

References

[1] S. Takaoka, H. Horikawa, J. Kobayashi, K. Shimizu, Mater. Sci. Forum 394–3 (2001) 61–68.
[2] N.B. Morgan, Mater. Sci. Eng. A 378 (2004) 16–23.
[3] T. Duerig, A. Pelton, D. Stöckel, Mater. Sci. Eng. A 273–275 (1999) 149–160.
[4] A. Sozinov, A.A. Likhachev, N. Lanska, K. Ullakko, Appl. Phys. Lett. 80 (2002) 1746–1748.
[5] K. Enami, S. Nenno, Metall. Mater. Trans. B 2 (1971) 1487–1490.
[6] K. Oikawa, L. Wulff, T. Iijima, F. Gejima, T. Ohmori, A. Fujita, K. Fukamichi, R. Kainuma, K. Ishida, Appl. Phys. Lett. 79 (2001) 3290–3292.
[7] Y. Murakami, D. Shindo, K. Oikawa, R. Kainuma, K. Ishida, Acta Mater. 50 (2002) 2173–2184.
[8] G.S. Firstov, J. Van Humbeeck, Y.N. Koval, J. Intell. Mater. Syst. Struct. 17 (2006) 1041–1047.
[9] R. Kainuma, M. Ise, C.C. Jia, H. Ohtani, K. Ishida, Intermetallics 4 (Supplement 1) (1996) S151–S158.
[10] K. Ishida, R. Kainuma, N. Ueno, T. Nishizawa, Metall. Mater. Trans. A 22 (1991) 441–446.
[11] R. Kainuma, S. Imano, H. Ohtani, K. Ishida, Intermetallics 4 (1996) 37–45.
[12] B. Bartova, D. Schryvers, Z. Yang, S. Ignacova, P. Sittner, Scripta Mater. 57 (2007) 37–40.
[13] W.H. Tian, M. Hibino, M. Nemoto, Intermetallics 6 (1998) 121–129.
[14] J. Kopeček, S. Sedláková-Ignácová, K. Jurek, M. Jarošová, J. Drahokoupil, P. Šittner, V. Novák, ESOMAT 02013 (2009).
[15] R. Yang, J.A. Leake, R.W. Cahn, J. Mater. Res. 6 (1991) 343–354.
[16] D.R. Hamilton, R.G. Seidensticker, J. Appl. Phys. 31 (1960) 1165–1168.
[17] J.-W. Lee, N.M. Hwang, D.-Y. Kim, J. Cryst. Growth 250 (2003) 538–545.
[18] J.-W. Lee, U.-J. Chung, N.M. Hwang, D.-Y. Kim, Acta Crystallogr. A 61 (2005) 405–410.
[19] O. Dmitrieva, D. Ponge, G. Inden, J. Millán, P. Choi, J. Sietsma, D. Raabe, Acta Mater. 59 (2011) 364–374.
[20] D.P. Cole, H.A. Bruck, A.L. Roytburd, Strain 45 (2009) 232–237.
[21] S. Cao, M. Nishida, D. Schryvers, Acta Mater. 59 (2011) 1780–1789.
[22] S. Cao, W. Tirry, W. Van Den Broek, D. Schryvers, J. Microsc. 233 (2009) 61–68.
[23] S.Q. Xiao, S. Hinderberger, K.H. Westmacott, U. Dahmen, Philos. Mag. A 73 (1996) 1261–1278.
[24] B. Bartova, N. Wiese, D. Schryvers, J.N. Chapman, S. Ignacova, Acta Mater. 56 (2008) 4470–4476.
[25] C.S. Oh, C.S. Han, C.H. Chun, K.W. Koo, J.W. Kim, Y.W. Kim, S.O. Han, C.H. Bae, J.H. Lee, Met. Mater. Int. 16 (2010) 175–183.
[26] W. Tirry, D. Schryvers, Nat. Mater. 8 (2009) 752–757.
[27] W. Tirry, D. Schryvers, Acta Mater. 53 (2005) 1041–1049.
[28] J. Kopeček, K. Jurek, M. Jarošová, J. Drahokoupil, S. Sedláková-Ignácová, P. Šittner, V. Novák, Mater. Sci. Eng. 7 (2010) 012013.
[29] Z. Yang, W. Tirry, D. Lamoen, S. Kulkova, D. Schryvers, Acta Mater. 56 (2008) 395–404.
[30] L. Bataillard, J.E. Bidaux, R. Gotthardt, Philos. Mag. A 78 (1998) 327–344.
[31] H. Shi, S. Pourbabak, J. Van Humbeeck, D. Schryvers, Scripta Mater. 67 (2012) 939–942.